Research Square

Preprints are preliminary reports that have not undergone peer review.
They should not be considered conclusive, used to inform clinical practice,
or referenced by the media as validated information.

Near-Infrared (1050 nm) Light-Driven Molecular Cobalt Photocatalysis

Youngmin You

odds2@yonsei.ac.kr

Yonsei University

Byung Hak Jhun

Yonsei University

Jihoon Jang

Chung-Ang University

Gyeong Min Park

Seoul National University

Seoyeon Kim

Yonsei University

Jin Yeong Choi

Seoul National University

Mi Sook Seo

Seoul National University https://orcid.org/0000-0003-3302-2508

Yubin Choi

Yonsei University

Sohee Lee

Yonsei University

Eun Jin Cho

Chung-Ang University https://orcid.org/0000-0002-6607-1851

Yunho Lee

Seoul National University https://orcid.org/0000-0002-9113-9491

Physical Sciences - Article

Keywords:

Posted Date: March 17th, 2026

DOI: https://doi.org/10.21203/rs.3.rs-8879727/v1

License: This work is licensed under a Creative Commons Attribution 4.0 International License.
Read Full License

Additional Declarations: There is **NO** Competing Interest.

Near-Infrared (1050 nm) Light-Driven Molecular Cobalt Photocatalysis

Byung Hak Jhun,† Jihoon Jang,† Gyeong Min Park, Seoyeon Kim, Jin Yeong Choi, Mi Sook Seo, Yubin Choi, Sohee Lee, Eun Jin Cho, Yunho Lee,* and Youngmin You**

Dr. Byung Hak Jhun, Seoyeon Kim, Yubin Choi, Sohee Lee, and Prof. Dr. Youngmin You
Department of Chemical and Biomolecular Engineering, Yonsei University, Seoul 03722, Republic of Korea
E-mail: odds2@yonsei.ac.kr

Gyeong Min Park, Jin Yeong Choi, Dr. Mi Sook Seo, and Prof. Dr. Yunho Lee
Department of Chemistry, Seoul National University, Seoul 08826, Republic of Korea
E-mail: yunhochem@snu.ac.kr

Jihoon Jang and Prof. Dr. Eun Jin Cho
Department of Chemistry, Chung-Ang University, Seoul 06974, Republic of Korea
E-mail: ejcho@cau.ac.kr

†These authors contributed equally to this work.

ABSTRACT

Photocatalysis has revolutionized synthetic chemistry; however, the reliance of exciting photocatalysts on high-energy photons limits the practical applications of this approach. Development of molecular photocatalysts that can be activated by near-infrared (NIR) light would fundamentally broaden the scope of photocatalysis. Here, we report a radical-featured cobalt complex that catalyzes the aerobic oxidation of benzylamines under 1050-nm irradiation—the longest wavelength ever recorded for a homogeneous molecular photocatalyst. This NIR light-driven photocatalysis was shown to remain efficient in large-volume reactions and turbid media, and to show wavelength-orthogonal tandem reactivity, highlighting its advantages over ultraviolet/visible light-driven photocatalysis. Mechanistic investigations based on spectroscopic measurements and quantum chemical calculations revealed a unique mechanism in which substrate-mediated hydrogen-atom transfer generates a light-active species that sustains NIR-driven turnover. Operating at the longest wavelength reported for a molecular photocatalyst, the platform establishes a distinct design principle for accessing photocatalytic reactivity beyond the traditional visible-light limit of homogeneous catalysts.

INTRODUCTION

Photocatalysis has emerged as a powerful tool for chemical syntheses because it can unlock reaction intermediates that are inaccessible under thermal conditions. When a photocatalyst absorbs photons, it transitions to an excited state with strong redox power and high electronic energy.[1-3] This excited-state catalyst rapidly reacts with substrates to generate highly reactive intermediates. Unlike thermal catalysis, the overall photocatalytic reaction is steered by the initial photoexcitation event, making the photon utilization the primary driver of reactivity.

Photocatalysis has several features that have reshaped contemporary synthetic chemistry.[4] Because photons function as a high-energy yet benign input, photocatalytic reactions can proceed under mild reaction conditions, typically with reduced by-product formation and enhanced chemoselectivity.[5-11] In addition, precise spatiotemporal control over reactivity can be achieved by modulating the light delivered to the reaction, enabling synergy with continuous flow reaction platforms.[12,13] Moreover, the tunability of photocatalyst absorption profiles broadens the utility of the catalysis.[14-17] Collectively, these capabilities position photocatalysis as a powerful and versatile tool for expanding the scope of chemical transformations.

The vast majority of reports on photocatalysis describe molecular systems activated by ultraviolet (UV) or visible (Vis) photons.[18,19] As summarized in Fig. 1, most photocatalysts studied to date absorb light at wavelengths shorter than 670 nm, leaving the near-infrared (NIR) region underexploited (see Supplementary Table 1 for a detailed summary).[20-34] The limited number of NIR-activatable photocatalysts include the use of expensive late-transition metal complexes,[35-37] phthalocyanine-derived structures,[38,39] and charged polymethine-type organic dyes,[40-42] as well as intricate photon up-conversion processes.[43-48] However, these strategies often suffer from constraints related to efficiency and synthetic generality. Nevertheless, the use of NIR photons for photocatalysis offers distinct advantages. In particular, the longer wavelength of NIR light allows it to penetrate further into scattering media, enhancing its performance in turbid reaction solutions and even in the complex biological milieu.[28,49-52] This ability to penetrate deep into media has implications for industrial photoreactors, which suffer from practical limitations related to high optical densities severely attenuating UV or Vis light and hence compromising reaction efficiency. Furthermore, NIR activation substantially broadens the accessible substrate space by minimizing competitive photochemical reactions of π-conjugated molecules. Collectively, these advantages underscore the compelling need for NIR-activatable photocatalysts.

Efforts to develop NIR photocatalysts face fundamental challenges. NIR photons possess insufficient energy to populate the excited states required to achieve the redox potentials or electronic energies necessary for substrate activation. Consequently, most molecular photocatalysts that are activated by UV and/or Vis light are not reactive when irradiated at NIR wavelengths. Although heterogeneous systems such as metal oxide nanoparticles,[53] low-dimensional semiconducting materials,[54] and plasmonic platforms[55] have shown reactivity under NIR photoirradiation, their performance typically relies on interfacial charge separation or localized heating under high-power excitation, and the underlying mechanisms tend to be poorly understood at the molecular level. Researchers have yet to develop robust molecular photocatalysts capable of harvesting

NIR photons to mediate synthetically valuable reactions. Development of such photocatalysts would establish a new regime of photocatalysis, broadening reactivity manifolds to areas that are inaccessible to current photocatalysis systems.

Transition metal complexes offer unique platforms for wavelength-tunable photocatalysts because their excited states can be systematically engineered through variation of the metal center,[56-58] ligand structure,[59-61] coordination geometry,[62,63] and metal–ligand covalency.[64-66] In this context, first-row transition metal complexes are especially attractive because they are earth-abundant, cost-effective, and display rich electronic transitions comprising ligand-to-metal charge-transfer (LMCT), metal-to-ligand charge-transfer (MLCT), and spin-flip transitions.[67] Despite these advantages, first-row transition metal complexes have been largely dismissed as candidates for NIR photocatalysis,[32-34] owing to two coupled limitations: i) their excited states are typically short-lived due to rapid quenching through low-lying metal-centered ligand-field states, and ii) few ligand scaffolds have been identified that have sufficiently low electronic energies along with robust and well-defined coordination.[68] As a result of these limitations, NIR-activatable molecular photocatalysts based on first-row transition metal complexes have been underdeveloped.

In this research, we establish a new strategy for NIR photocatalysis based on an octahedral Co(III) complex. The Co complex incorporates two tridentate C∧N∧C ligands possessing an amido (N) and *N*-heterocyclic carbene (C) donors, where one is monoanionic (i.e., C∧N^-∧C) and the other has an unpaired electron at the central N moiety (i.e., C∧N•∧C) (Fig. 1). The radical species is substantially stabilized through full delocalization over the [(C∧N^-∧C)Co(III)(C∧N•∧C)]$^{2+}$ coordination framework, denoted as [**Co**]$^{2+}$ hereinafter. This delocalization dramatically narrows the optical bandgap, enabling intense and continuous absorption that goes beyond the NIR-II region and reaches into the mid-infrared (MIR) regime, remaining detectable out to ca. 3.0 μm. The [**Co**]$^{2+}$ complex is shown to efficiently catalyze the aerobic oxidative coupling of benzylamine to the corresponding *N*-benzylidenebenzylamine under NIR-II irradiation at 1050 nm. To the best of our knowledge, this constitutes the longest-wavelength activation yet demonstrated for a molecular photocatalyst.

A key conceptual advance of this study is the use of a first-row transition-metal complex that derives its reactivity from a radical unit, enabling access to two distinct activation pathways. We demonstrate that the [**Co**]$^{2+}$ complex operates as a dual-mode catalyst for substrate activation, engaging in spontaneous hydrogen-atom transfer (HAT) in the dark state followed by NIR-induced unlocking of a photoinduced electron-transfer (PeT) pathway. This duality arises from the synergistic interaction between the Co(III) center and the radical C∧N•∧C ligand. We show that the NIR-activatable cobalt photocatalyst still promotes efficient transformations when the reaction volume is large and maintains high reactivity in strongly scattering, heterogeneous media, conditions under which Vis-light-activatable photocatalysts perform poorly. The long-wavelength activation further enables photoorthogonal transformations and two-wavelength tandem photocatalytic sequences, illustrating the breadth of reactivity accessible under NIR illumination. Mechanistic analyses combining femtosecond transient absorption spectroscopy, electrochemical studies, and quantum chemical calculations support a coherent mechanistic framework consistent with these reactivity manifolds.

Collectively, these findings establish NIR-responsive molecular photocatalysis as a promising direction. We anticipate that the results obtained in this research will stimulate the development of a broader family of NIR-activatable molecular photocatalysts.

RESULTS

NIR photocatalysis

We first probed the wavelength dependence of the [**Co**]$^{2+}$ complex-mediated photocatalytic aerobic oxidation of benzylamine (**1a**) as a model substrate in acetonitrile (CH_3CN) under an O_2 atmosphere (Table 1). The [**Co**]$^{2+}$ complex exhibited robust activity upon NIR excitation, with irradiation at 850 nm furnishing the imine product, *N*-benzylidenebenzylamine (**1b**), in yields comparable to those obtained under UV- or Vis-light irradiation at 405 and 650 nm in the presence of [**Co**]$^{2+}$ (Table 1, entries 2–4). Notably, catalytic activity was still observed even when the excitation wavelength was extended to 1050 nm, albeit with a slight decrease in efficiency (entry 1). Further increase of the wavelength to 2800 nm, however, resulted in no detectable product formation (entry 5). Control experiments confirmed that molecular oxygen, light irradiation, and [**Co**]$^{2+}$ were all required for the oxidation reaction to proceed (entries 6–8), thereby establishing the photocatalytic nature of the transformation.

To assess the substrate generality of the NIR-activated [**Co**]$^{2+}$-catalyzed aerobic oxidation under 1050 nm irradiation, we performed experiments using a range of substituted benzylamines as the substrate (Table 2). Benzylamine derivatives bearing electron-withdrawing substituents, including halogens (**2a**, **3a**, **4a**, and **5a**) and trifluoromethyl (**6a**, **7a**, and **8a**) or trifluoromethoxy groups (**9a**), were smoothly transformed into the corresponding *N*-benzylidenebenzylamine products. Electron-donating substituents were likewise well tolerated. Substrates containing methyl (**10a**, **11a**, and **12a**) or methoxy (**13a**) groups underwent efficient oxidation without noticeable erosion of reactivity. Moreover, when a similar experiment was performed on the heteroaromatic substrate pyridin-3-ylmethanamine (**14a**), the corresponding imine product (**14b**) was obtained, indicating the generality of the reaction beyond simple arenes.

Next, we assessed the practical scope and functional advantages of the catalyst (Fig. 2). We first evaluated the scalability of the benzylamine oxidative coupling reaction under NIR illumination. A large-volume reaction was conducted in a 500 mL round-bottom flask (diameter, 13 cm) containing 300 mL of CH_3CN, 25 mmol of **1a**, and 0.1 mol% of [**Co**]$^{2+}$ under aerobic conditions. The reaction mixture was irradiated with an array of 1050 nm LEDs (3 W). Importantly, because [**Co**]$^{2+}$ was the only reaction component that exhibits absorption at this wavelength, unintended light absorption by the reaction solution did not occur. Under these conditions, the product **1b** was obtained in 65% yield (Fig. 2a), demonstrating that efficient photocatalysis could be sustained over a long optical path length. Thus, the NIR-activatable cobalt photocatalyst is suitable for use in large-scale reactors in which visible-light penetration is inherently limited.

As a second demonstration, we examined the performance of the NIR photocatalyst in a heterogeneous medium. To create a turbid reaction environment, chemically inert yttria-stabilized zirconia (Y:Zr) particles (average diameter ~700 nm) were dispersed in the reaction mixture. At loadings above 0.05

wt%, the suspension became cloudy and strongly scattered Vis light (Fig. 2b). Under such conditions, photocatalysts requiring visible excitation exhibit severely diminished activity. In contrast, [**Co**]$^{2+}$ maintained substantial catalytic efficiency under 1050-nm illumination, affording **1b** in 72% yield. This result directly reflects the greater penetration depth of NIR photons in heterogeneous media and demonstrates a key advantage of NIR photocatalysis over conventional Vis-light-driven systems.

Because many π-conjugated organic molecules show limited absorption of NIR photons, selective activation of the [**Co**]$^{2+}$ catalyst can still be achieved in systems containing π-conjugated components. To explore this concept, we synthesized a biscyclometalated Ir(III) complex bearing an aminomethylene substituent (**15a**). This Ir(III) complex displays strong absorption bands in the UV and blue regions, making it a potential photocatalyst under Vis-light irradiation[69] (Fig. 2c). In the presence of [**Co**]$^{2+}$ under 1050-nm irradiation, however, oxidative coupling of this Vis-active Ir(III) complex generated the corresponding Ir(III) dyad (**15b**) (78%). Notably, the dyad product retained the intrinsic photophysical properties of the Ir(III) chromophore (Supplementary Fig. 1), illustrating that the NIR photocatalysis enables chemoselective functionalization without perturbing the Vis-light-response of the molecule.

Finally, we designed photoorthogonal sequential tandem photocatalytic reactions that exploit wavelength-selective catalyst activation. An aerated CH_3CN solution containing 0.1 mmol **1a**, 1 mol% [**Co**]$^{2+}$, and 1 mol% $[Ru(bpy)_3]^{2+}$ (bpy = 2,2′-bipyridine) was first irradiated at 1050 nm to generate **1b** selectively via cobalt-catalyzed NIR activation. Subsequent illumination of the same reaction mixture at 450 nm, in the presence of a Hantzsch ester, triggered Ru-catalyzed photoreduction[70] to afford dibenzylamine (**1c**) in an overall yield of 56% (Fig. 2d). This sequential process demonstrates precise wavelength-gated control over two distinct catalytic cycles within a single reaction vessel.

Collectively, the above demonstrations of the suitability of NIR-activatable [**Co**]$^{2+}$ for large reaction volumes, turbid media, selective functionalization of a Vis-light-active substrate, and photoorthogonal tandem catalysis highlight the distinctive reactivity space that can be accessed by using [**Co**]$^{2+}$ and establish its strong potential for practical and modular photocatalytic syntheses.

Identification of photocatalytic species

The [**Co**]$^{2+}$ complex exhibited a deep blue color in CH_3CN, but the color instantly changed to green upon addition of **1a** (see the inset photo in Fig. 3a). This pronounced colorimetric response suggests a light-independent, dosimetric reaction between [**Co**]$^{2+}$ and **1a**. As shown in Fig. 3a, the Vis–NIR absorption spectrum of 1.0 mM [**Co**]$^{2+}$ displayed intense absorption bands in both the visible (< 750 nm) and NIR-to-MIR (1050–3200 nm) regions, the latter originating from the delocalized ligand-centered radical character of the complex (see Supplementary Tables 2–10 for the assignments based on quantum chemical calculations and Supplementary Fig. 2 for spin densities). Introducing 100 mM **1a** caused a hypochromic shift in the visible bands and almost complete disappearance of the NIR-to-MIR feature of [**Co**]$^{2+}$, indicating loss of the radical signature and formation of a diamagnetic species.

Electrospray ionization mass spectrometry (positive mode) data further corroborated this transformation (Fig. 3b). The mixture of $[\mathbf{Co}]^{2+}$ and **1a** exhibited a base peak at m/z = 386.16, which corresponds to an increase of ca. 0.50 amu relative to the parent $[\mathbf{Co}]^{2+}$ complex (m/z = 385.59). This result is consistent with the formation of a hydrogen-atom adduct, $[\mathbf{Co–H}]^{2+}$. Formation of $[\mathbf{Co–H}]^{2+}$ is supported by the observation that, when the same reaction was performed using deuterated benzylamine ($PhCD_2NH_2$), a ca. 1.0 amu increase (m/z = 386.56) was observed, consistent with formation of the deuterium-atom adduct, $[\mathbf{Co–D}]^{2+}$.

Spectroscopic analysis of absorption signals provides additional validation for the generation of $[\mathbf{Co–H}]^{2+}$. The difference absorption spectrum comparing $[\mathbf{Co}]^{2+}$ before and after **1a** addition shows diminishment of the characteristic visible absorption of $[\mathbf{Co}]^{2+}$ and the emergence of a new band in the NIR-II region (900–1400 nm) (Fig. 3c). Quantum-chemical calculations at the UB3LYP/def2-SVP level of theory attributed this new NIR-II feature to an MLCT transition of $[\mathbf{Co–H}]^{2+}$ (Fig. 3d and Supplementary Fig. 3). The possibility that a redox change contributes to this signal can be excluded based on the observation that the Vis–NIR absorption spectra of independently prepared $[\mathbf{Co}]^{+}$ and $[\mathbf{Co}]^{3+}$ differed markedly from that of $[\mathbf{Co–H}]^{2+}$ (Supplementary Fig. 4). Additional FT–IR and Raman spectroscopic experiments aimed at testing for the newly formed H–N–Co bond were unsuccessful due to substantial overlaps with **1a** peaks. However, the primary kinetic isotope effect (KIE) value of 2 strongly supports the involvement of HAT (Fig. 3e): $[\mathbf{Co}]^{2+}$ + $PhCH_2NH_2 \rightarrow [\mathbf{Co–H}]^{2+}$ + $PhC{\bullet}HNH_2$. Together, these results demonstrate that $[\mathbf{Co}]^{2+}$ undergoes a spontaneous, light-independent HAT reaction with **1a** to generate the diamagnetic $[\mathbf{Co–H}]^{2+}$ species and the radical species of benzylamine (i.e., $PhC{\bullet}HNH_2$) that constitutes the activated form of the substrate.

Importantly, $[\mathbf{Co–H}]^{2+}$ is identified as the key photoactive species in the catalytic cycle. As shown in Fig. 3f, the wavelength-dependent photochemical action profile shows the highest reaction quantum yield (Φ_r) at a wavelength of 850 nm irradiation. NIR-II irradiation, which can selectively photoexcite $[\mathbf{Co–H}]^{2+}$, also displays a substantial contribution to Φ_r (0.4%). Notably, Φ_r values in the visible region (< 750 nm) are similar to or lower than those observed in the NIR regime, indicating that long-wavelength photoexcitation more efficiently drives the photocatalytic reaction. Note that the closed-shell $[\mathbf{Co–H}]^{2+}$ species can form a singlet excited state that is longer-lived than the doublet excited state of $[\mathbf{Co}]^{2+}$ (see below). This change in spin state, thus, improves the photocatalytic performance.

Photocatalysis mechanism

Having identified the catalytically competent photoactive species, we sought to elucidate the mechanism underlying the photocatalysis. Because molecular oxygen is indispensable for the reaction, we focused on excited-state interactions between O_2 and $[\mathbf{Co–H}]^{2+}$. We subjected 2.0 mM $[\mathbf{Co}]^{2+}$ in deaerated CH_3CN without **1a** to femtosecond pulsed laser excitation at 550 nm, and recorded the transient Vis–NIR absorption spectra (Figs. 4a and d). A strong positive photoinduced absorption (PIA) band centered at 732 nm appears immediately after excitation and decays rapidly with a lifetime of τ = 9.0 ps (Fig. 4g). This transient state is

assigned to a doublet metal-to-ligand charge-transfer (^{2}MLCT) transition excited state of the radical $[\mathbf{Co}]^{2+}$ species. The ultrafast decay of the PIA band is consistent with a spin-allowed doublet–doublet relaxation pathway, rendering this excited state kinetically ineffective for interaction with O_2.

In presence of **1a**, by contrast, qualitatively distinct excited-state dynamics are observed. Femtosecond transient absorption spectra acquired from a solution containing 2.0 mM $[\mathbf{Co}]^{2+}$ and 200 mM **1a** reveal a new, weak PIA band at 677 nm in addition to the 732-nm feature (Figs. 4b and e). Notably, the 677-nm band persists beyond the temporal window (> 5 ns), indicating the formation of a substantially longer-lived excited state. Nanosecond transient absorption measurements confirm a lifetime of $\tau = 3.9$ ns for this state (Figs. 4h and i). The pronounced lifetime elongation is consistent with the singlet excited state, and the 677 nm transient is therefore assigned to a singlet MLCT (^{1}MLCT) state of $[\mathbf{Co}–\mathbf{H}]^{2+}$.

The emergence of this singlet excited state in the presence of **1a** is mechanistically critical. Unlike the ^{2}MLCT state of $[\mathbf{Co}]^{2+}$, the ^{1}MLCT state of $[\mathbf{Co}–\mathbf{H}]^{2+}$ ($[\mathbf{Co}–\mathbf{H}]^{2+}$*) is long-lived, and hence kinetically compatible with oxidative quenching by O_2: $[\mathbf{Co}–\mathbf{H}]^{2+}$* + $O_2 \rightarrow [\mathbf{Co}–\mathbf{H}]^{3+} + O_2^{\bullet-}$. Upon O_2 saturation, the decay of the 677 nm PIA signal is markedly accelerated, with a reduced lifetime of $\tau = 1.0$ ns, and a new PIA feature appears at approximately 860 nm (Figs. 4c, f and i). This band can be assigned to the one-electron-oxidized cobalt species, $[\mathbf{Co}–\mathbf{H}]^{3+}$, on the basis of the close agreement with electronic transition spectra simulated at the UB3LYP/def2-SVP level of theory (Supplementary Fig. 3). Thermodynamic analysis also reveals that PeT from $[\mathbf{Co}–\mathbf{H}]^{2+}$* to O_2 is favorable, with a free energy change of −0.57 eV (Supplementary Figs. 5 and 6). In contrast, analogous PeT from excited-state $[\mathbf{Co}]^{2+}$ ($[\mathbf{Co}]^{2+}$*) is disfavored, because it exhibits a positive free energy change of 0.62 eV. Independent corroboration of the photoinduced reduction of O_2 is provided by the turn-on response of a fluorescence-based superoxide dosimeter, which selectively detects $O_2^{\bullet-}$ generated under irradiation (Supplementary Fig. 7). Together, these results demonstrate that oxidative quenching of $[\mathbf{Co}–\mathbf{H}]^{2+}$* by O_2 is the key productive photochemical step.

The rate of PeT (k_{PeT}) was determined from the relation $k_{PeT} = 1/\tau(O_2) - 1/\tau(Ar)$, where $\tau(O_2) = 1.0$ ns and $\tau(Ar) = 3.9$ ns correspond to the decay lifetimes of the 677 nm PIA signal in the presence and absence of O_2, respectively. This analysis yields $k_{PeT} = 7.4 \times 10^8$ s^{-1}, which exceedes the intrinsic excited-state decay rate of $[\mathbf{Co}–\mathbf{H}]^{2+}$* ($k_d$, $k_d = 1/\tau(Ar) = 2.6 \times 10^8$ s^{-1}) by approximately a factor of three, demonstrating efficient electron transfer. We propose that, following electron transfer, a proton-transfer event occurs within the resulting geminate radical-ion pair $[[\mathbf{Co}–\mathbf{H}]^{3+} \cdots O_2^{\bullet-}]$, generating a $[[\mathbf{Co}]^{2+} \cdots HOO\bullet]$ species. Subsequent dissociation releases free $[\mathbf{Co}]^{2+}$ and HOO• species, thereby closing the photocatalytic cycle. Competing back-electron transfer within the geminate radical-ion pair to regenerate $[\mathbf{Co}–\mathbf{H}]^{2+}$ and O_2 is also possible. Although direct spectroscopic observation of regenerated $[\mathbf{Co}–\mathbf{H}]^{2+}$ was precluded by signal-to-noise limitations, the lifetime of the $[\mathbf{Co}–\mathbf{H}]^{3+}$ species was significantly prolonged in the presence of excess TEMPOL, a superoxide anion scavenger (Supplementary Fig. 8), providing indirect evidence for back electron transfer.

DISCUSSION

Our study resolves two long-standing challenges in developing NIR-activatable molecular photocatalysts: i) intrinsically low energies and ii) short lifetime of their excited states. By integrating a ligand-centered radical into an octahedral cobalt framework, we achieve unprecedented NIR light-driven photocatalytic activities. This design principle contrasts sharply with previous approaches relying on expensive late-transition metal complexes, charged organic dyes, and photon up-conversion, demonstrating a fundamentally new strategy for long-wavelength molecular photocatalysis. Our mechanistic investigations reveal the dual activation of substrates by an NIR-activatable photocatalyst. As shown in Scheme 1, the $[\mathbf{Co}]^{2+}$ complex bearing the radical C∧N•∧C ligand interacts with **1a** in its ground state. This interaction activates **1a** by abstracting a hydrogen atom to form the putative PhC•HNH_2 intermediate and closed-shell $[\mathbf{Co–H}]^{2+}$ species. The $[\mathbf{Co–H}]^{2+}$ complex can absorb NIR photons to form its singlet excited state, which is longer-lived than the doublet excited-state of $[\mathbf{Co}]^{2+}$. The intrinsic decay rate of the singlet excited-state $[\mathbf{Co–H}]^{2+}$ species is 2.6×10^8 s^{-1}. This decay rate is on the same order of the diffusion rate of 0.01 M cobalt complex in acetonitrile at 298 K[71] ($0.01\ M \times 1.9 \times 10^{10}\ M^{-1}\ s^{-1} = 1.9 \times 10^8\ s^{-1}$), providing ample possibility for interaction between singlet excited-state $[\mathbf{Co–H}]^{2+}$ and O_2. The excited-state $[\mathbf{Co–H}]^{2+}$ complex is oxidatively quenched by O_2 at a rate of 7.4×10^8 s^{-1} to form the geminate radical ion pair of $[[\mathbf{Co–H}]^{3+} \cdots O_2^{\bullet-}]$. We hypothesize that rapid proton transfer occurs within the geminate radical ion pair, leading to dissociation into the ground-state $[\mathbf{Co}]^{2+}$ and HOO•. Note that this photocatalytic cycle mediated by $[\mathbf{Co–H}]^{2+}$ leads to activation of the second substrate, O_2. It is plausible that radical recombination between HOO• and PhC•HNH_2 may occur to form the hydroperoxyl adduct of **1a**. Finally, elimination of H_2O_2 from the adduct produces an imine intermediate[72] which subsequently reacts with another **1a** molecule to form the desired product **1b**.

The present research establishes a new paradigm for NIR-activatable molecular photocatalysis. The cobalt complex reported here circumvents the intrinsic limitation of utilizing NIR photons in photocatalysis, namely that such photons have insufficient energy to populate excited states required to substrate activation. It does this by dividing the activation of the substrate into two synergistic steps: light-independent hydrogen-atom transfer that generates a benzyl radical intermediate of the substrate with the closed-shell, NIR-absorbing cobalt complex, followed by NIR-driven electron transfer that activates molecular oxygen. This two-step process enables photocatalysis at the unprecedented photoirradiation wavelength of 1050 nm. The resulting NIR photocatalysis exhibits a set of practical capabilities that are inaccessible to conventional UV–Vis photocatalyst systems, including efficient operation in large-volume reactors and strongly scattering heterogeneous media, photoselective functionalization of visible-light-active chromophores, and photoorthogonal tandem catalysis. Beyond the NIR photocatalysis demonstrated here, mechanistic investigations uncovered the unique photophysical processes underlying the photocatalysis. Finally, $[\mathbf{Co}]^{2+}$ remains stable under continuous NIR photoirradiation (Supplementary Fig. 9). We anticipate that this work will drive the development of a broader class of earth-abundant, NIR-responsive molecular photocatalysts and open new opportunities for photocatalytic organic transformations under conditions that are incompatible with existing photocatalysis systems.

METHODS

Synthesis of* [Co]$^{2+}$ *complex. The dicationic complex [**Co**]$^{2+}$ was synthesized using a modified version of a previously reported procedure.[73] To a slurry of **H_3CNC-PF_6** ligand (200 mg, 0.308 mmol) in 20 mL of THF, $CoBr_2$ (34 mg, 0.154 mmol) was added. After cooling the mixture to –78 °C, LiHMDS (0.94 mL, 1.0 M in THF, 0.94 mmol) was added dropwise. The reaction mixture was then warmed to room temperature and stirred for 4 h. The resulting green solution was dried under vacuum, and the residue was washed with pentane (5 mL). After washing, the residue was dissolved in dichloromethane (20 mL) and the solution was filtered through a celite pad on a glass frit. $NaPF_6$ (65 mg, 0.385 mmol) was added to the collected filtrate solution, and the resulting green solution was stirred for 4 h under an O_2 atmosphere to furnish a blue solution. This blue solution was extracted with dichloromethane (100 mL × three times), dried over anhydrous Na_2SO_4 and filtered to collect the dried organic phase. After all volatiles were removed under vacuum, the resulting mixture was crashed out with CH_3CN and diethyl ether. After drying under vacuum, [**Co**]$^{2+}$ was obtained as a blue solid (100 mg, 0.0939 mmol, 60.9 %). The synthesized product was characterized by ^{1}H NMR and ESI-MS data and assigned by comparing with [**Co**]$^{2+}$ data from the previous report.

Synthesis of* [Co]$^{+}$ *complex. The monocationic complex [**Co**]$^{+}$ was synthesized according to the previously reported procedure.[73] The synthesized product was characterized by ^{1}H NMR and ESI-MS data and assigned by comparing with [**Co**]$^{+}$ data from the previous report.

Synthesis of* [Co]$^{3+}$ *complex. Magic blue – PF_6 ($(BrC_6H_4)_3NPF_6$, 88 mg, 0.141 mmol), dissolved in CH_3CN (10 mL), was added to a solution of [**Co**]$^{2+}$ (100 mg, 0.0939 mmol) dissolved in CH_3CN (20 mL). The reaction mixture was stirred for 1 h at room temperature and all volatiles were removed under vacuum. The resulting solid residue was sequentially washed with toluene (30 mL), pentane (10 mL), and dichloromethane (10 mL). A deep blue solid ([**Co**]$^{3+}$) was obtained in a 98% yield (116 mg, 0.0920 mmol). UV−vis [CH_3CN, nm (M^{-1} cm^{-1})]: 800 (7150), 630 (8270). ESI-HR-MS for $[C_{44}H_{44}N_{10}Co]^{3+}$: Calcd, 257.1022; Found, 257.1027; Anal. Calcd for $C_{44}H_{44}N_{10}F_{18}P_3Co{\cdot}2CH_3CN$: C, 44.73; H, 3.91; N, 13.04. Found: C, 44.72; H,4.33; N, 13.02. μ_{eff}: 1.74 μ_B (CD_3CN, 25 °C, Evans' method). X-ray quality crystals were grown by diffusion of diethyl ether into a saturated solution of [**Co**]$^{3+}$ in acetonitrile. Crystal data for [**Co**]$^{3+}$ (as obtained, CCDC 2524979): $C_{52}H_{56}CoF_{18}N_{14}P_3$, Monoclinic, *C*2/c, a = 33.469(6) Å, b = 18.220(3) Å, c = 19.705(3) Å, α = 90°, β = 98.822(7)°, γ = 90°, V = 11874(4) Å^3, Z = 8, ρ_{calcd} = 1.534 g cm^{-3}, μ = 0.477 mm^{-1}, F(000) = 5,600. Data collection: T = 100(2) K, θ_{range} = 2.236–24.498°, reflections collected = 131,455, independent reflections = 9,876 (R_{int} = 0.1202). Refinement: R_1 = 0.1095, wR_2 = 0.2909 for all data.

X-ray Crystallography. Single-crystal X-ray diffraction data for [**Co**]$^{3+}$ were collected using a Bruker D8 QUEST instrument at the Department of Chemistry of Seoul National University. A crystal of suitable size and quality was coated with Paratone-*N* oil and mounted on a Dual-Thickness MicroLoop LD purchased from MiTeGen. Data were collected with graphite-monochromated MoKα radiation (λ = 0.71073 Å) under a N_2(g) stream at 100 K. Cell parameters were determined and refined using the SMART program. Data reduction was performed using SAINT software. An empirical absorption correction was applied using SADABS software. The structures were solved by direct methods, and all non-hydrogen atoms were subjected to

anisotropic refinement by full-matrix least squares on F^2 by using the SHELXTL/PC package on the ShelXle graphical user interface. All hydrogen atoms were placed at their geometrically calculated positions and refined riding on the corresponding carbon atoms with isotropic thermal parameters. Reflection outliers |error/esd| > 10 of the structural models were omitted.

General methods for photocatalysis reactions. Benzylamine substrate (0.10 mmol), $[\mathbf{Co}]^{2+}$ (8.0 mg, 10 mol%), and anhydrous CH_3CN (1.0 mL) were placed in an oven-dried reaction vial equipped with a magnetic stir bar. The vial was sealed with a screw cap fitted with a PTFE/silicone septum, through which molecular oxygen was introduced for 10 min by bubbling *via* a needle connected to an oxygen balloon. The reaction mixture was then stirred under irradiation with 1050-nm LEDs (340 mW or 3 W). Upon completion of the reaction, as monitored by TLC and GC–MS, the solvent was removed under reduced pressure. The resulting residue was purified by flash column chromatography on silica gel using a mixture of hexanes and ethyl acetate containing 1 vol% triethylamine as an eluent.

Steady-state UV–Vis–NIR absorption measurements. UV−Vis−NIR absorption spectra of Co complexes were obtained on an Agilent, Cary 5000 spectrophotometer at 298 K. Sample solutions were prepared prior to measurements and delivered into a modified quartz cell (Hellma, beam path = 1 mm) with a gas adaptor joint. All sample solutions were prepared to a concentration of 1.0 mM in CD_3CN inside a glovebox and sealed with a rubber septum to prevent air exposure. Note that using a longer optical path length for solutions with CH_3CN as the solvent leads to C–H vibrational overtone signals, making it impossible to measure clear absorption signals. **1a** was also handled inside a glovebox, placed in a vial, and sealed with a rubber septum. Prior to transferring **1a** from the septum-sealed vial to the cuvette containing the $[\mathbf{Co}]^{2+}$ solution, both containers were connected to an Ar balloon to maintain air-free conditions. For O_2 bubbling, an O_2 balloon equipped with a needle was used to deliver O_2 into the cuvette through the rubber septum, while a second needle served as a vent/outlet. Bubbling was performed for 5–10 min. All mixing procedures were performed in the dark to eliminate effects related to light absorption.

Quantum chemical calculations. Quantum chemical calculations based on density functional theory (DFT) were performed using the Gaussian 16 package. Ground-state geometry optimization was carried out using the UB3LYP functional and the def2-SVP basis set for all atoms. Single-point calculations were performed for the optimized geometries using the TD-UB3LYP functional and the same basis set as that used in the geometry optimization. The conductor-like polarizable continuum model (CPCM) parameterized for CH_3CN was applied for both geometry optimization and single-point energy calculations. UV−Vis−NIR absorption spectra were simulated using the results from TD-DFT calculation through Gauss View 6.0 software. The spin-density calculated at the UB3LYP/def2-TZVPP level of theory. The electronic transitions were characterized by using hole and electron distribution analysis calculated with Multiwfn software,[74] following the reported method.[75] The hole and electron distributions were visualized by generating isosurface contours as gaussian cube file formats in Multiwfn. To analyze the population character of the electronic transition, the structure was separately fragmented as the metal center and the amido and carbene ligands.

Hydrogen atom transfer reactions. KIE was evaluated by time-resolved UV–Vis absorption measurements using an Agilent, Cary 300 spectrophotometer. A $[\mathbf{Co}]^{2+}$ solution was prepared at a concentration of 1.0 mM in CH_3CN. The sample was kept in an Ar atmosphere during measurements. Compound **1a** or $PhCD_2NH_2$ (0.5, 1.0, 2.0, or 5.0 mM) was then introduced into the $[\mathbf{Co}]^{2+}$ solution, and the absorbance change at 568 nm was recorded immediately after mixing. The KIE was determined by comparing the observed reaction rates observed at different concentrations of **1a** or $PhCD_2NH_2$ determined by pseudo-first order plots.

Electrochemical characterization. Cyclic voltammetry (CV) and differential pulse voltammetry (DPV) were performed using a CH Instruments, CHI630 B potentiostat with a three-electrode cell assembly. Pt wire and glassy carbon were used as the counter and working electrodes, respectively. An $Ag/AgNO_3$ couple was used as the pseudo-reference electrode. Measurements were carried out in Ar-saturated THF (2.0 mL) containing either 2.0 mM $[\mathbf{Co}]^{2+}$ or 12 mM **1a**, with 0.10 M $(n\text{-Bu})_4NPF_6$ as the supporting electrolyte at scan rates of 100 mV s^{-1} (CV) or 4.0 mV s^{-1} (DPV). All potentials were referenced externally to the ferrocenium/ferrocene couple. Electrochemical potentials for $[\mathbf{Co}\text{–}\mathbf{H}]^{2+}$ were estimated at the UB3LYP/def2-SVP level of theory using DFT methods in combination with a thermodynamic Born–Haber cycle.[76] The geometries of the neutral and one-electron oxidized states of $[\mathbf{Co}]^{2+}$, $[\mathbf{Co}\text{-}\mathbf{H}]^{2+}$, and ferrocene were optimized, after which frequency calculations were performed to obtain thermally corrected Gibbs free energies. Each state was calculated in the gas phase using the CPCM parameterized for CH_3CN. All potentials were evaluated as V vs normal hydrogen electrode (NHE) using the following equation:

$$E_{ox} = \frac{G^{\circ}(O) + n_p G^{\circ}(H^+) + n_p G^{\circ}(e^-) - G^{\circ}(N)}{n_e} - E^{\circ}_{NHE}$$

where $G°(O)$ is the free energy of the oxidized species, $G°(H^+)$ is the free energy of a proton, $G°(e^-)$ is the free energy of an electron, $G°(N)$ is the free energy of the neutral species, n_e is the number of electrons transferred, n_p is the number of protons transferred, and $E°_{NHE}$ is the standard potential of the normal hydrogen electrode. Here, $G°(e^-)$ is taken as 0 eV[77] and n_p is taken as 0 considering a simple oxidation reaction. The value of $E°_{NHE}$ is taken as 4.28 V.[78] The calculated oxidation potential of ferrocene was used as a standard to reference all computed potentials, which were then converted to values V vs saturated calomel electrode (SCE) values. The calculated potential of $[\mathbf{Co}\text{–}\mathbf{H}]^{2+}$ was further corrected by subtracting the difference between the calculated and experimental oxidation potentials of $[\mathbf{Co}]^{2+}$. The excited-state oxidation (E^*_{ox}) potentials were determined using the following equation.

$$E^*_{ox} = E_{ox} - \Delta E_g$$

where E_{ox}* is the excited-state oxidation potential, E_{ox} is the ground-state oxidation potential, and ΔE_g is the optical bandgap energy. Here, ΔE_g was approximated as the photon energy of 1050-nm LEDs because the broad and ambiguous absorption profile prevented a reliable determination of the onset wavelength.

Femtosecond-transient absorption measurements. Femtosecond transient absorption measurements were performed at the Korea Basic Science Institute (KBSI), Seoul Center. Ar-saturated CH_3CN solutions containing 2.0 mM $[\mathbf{Co}]^{2+}$ or both 2.0 mM $[\mathbf{Co}]^{2+}$ and 200 mM **1a** were prepared in an Ar-purged glovebox. Each solution was transferred to a modified 1 cm × 1 mm quartz cell equipped with a gas adaptor joint and

sealed with a rubber septum. Measurements were conducted in the absence and presence of O_2. Sample solutions were excited by a Yb:KGW femtosecond amplifier system (Light Conversion, 200 kHz, 20 W). The samples were excited with a femtosecond pulsed laser at 550 nm (130 μW), and the transient absorption spectra were recorded using a broadband white-light probe spanning the range 580–900 nm. The data were collected with a time resolution sufficient to capture ultrafast processes over a 0–5000 ps window. All experiments were performed at 298 K. The decay profiles of the photoinduced absorption were fit by nonlinear least-squares analysis to a monoexponential decay model using OriginLab, OriginPro 2025 software.

Nanosecond laser flash photolysis. An Ar-saturated CH_3CN solution containing both 2.0 mM [**Co**]$^{2+}$ and 200 mM **1a** was prepared in an Ar-purged glovebox. The sample was transferred to a modified 1 × 1 cm quartz cell equipped with a gas adaptor joint and sealed with a rubber septum, and measurements were carried out in the absence and presence of O_2. Sample solutions were excited using a Nd:YAG laser (Continuum, SLII-10) at a wavelength of 532 nm with an energy of 5 mJ pulse^{-1}. Transient absorption kinetics were recorded using a Hamamatsu R2949 photomultiplier tube (Vis region)/InGaAs-PIN photodiode (NIR region) as detectors. The outputs from the detectors were acquired using a Tektronix, TDS3032 (300 MHz) digitized oscilloscope. All experiments were performed at 298 K. The decay traces of the photoinduced absorption at 660 nm were fit by nonlinear least-squares analyses to a monoexponential decay model using OriginLab, OriginPro 2025.

DATA AVAILABILITY

Raw data supporting the findings of this study are available from the authors upon reasonable request. Source data are provided with this paper and supplementary information.

ACKNOWLEDGMENTS

This work was supported by National Research Foundation grants (RS−2023-00208856 to Y.Y.; RS-2025-00559692 to E.J.C; 2022M3C1A3092056 to Y.L.) funded by the Ministry of Science, Information, and Communication Technology (ICT) and Future Planning (MSIP) of Korea. Y.Y. also acknowledges the financial support from a grant funded by the Ministry of Trade, Industry and Energy of Korea (RS-2024-00441743).

AUTHOR CONTRIBUTIONS

B. H. J. and J. J. contributed equally to this work. B. H. J. conducted spectroscopic experiments and quantum chemical investigations, analyzed the data, and wrote the manuscript. J. J. designed and synthesized the substrates, and evaluated the catalytic performance. G. M. P., J. Y. C., and M. S. S. synthesized cobalt complexes and performed the structural characterization. S. K., Y. C., and S. L. performed spectroscopic measurements and evaluated the NIR photocatalytic activity. E. J. C. supervised the research at Chung-Ang University and co-wrote the manuscript. Y. L. supervised the synthesis and structural characterization of cobalt complexes at Seoul National University and co-wrote the manuscript. Y. Y. coordinated all experiments and co-wrote the manuscript.

CONFLICTS OF INTEREST

The authors declare no competing interests.

REFERENCES

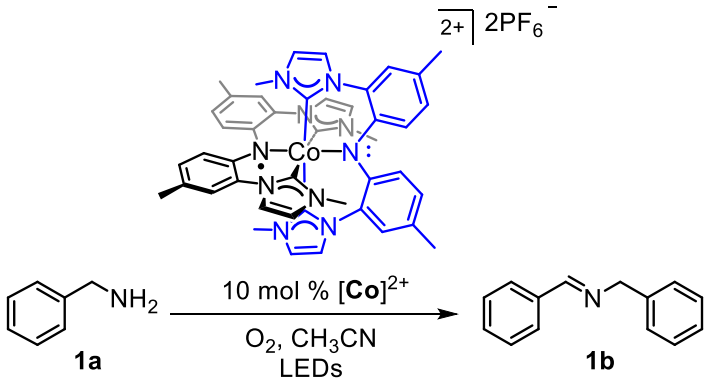
1 MacMillan, D. W. C. The advent and development of organocatalysis. *Nature* **455**, 304–308 (2008).
2 Schultz, D. M. & Yoon, T. P. Solar synthesis: prospects in visible light photocatalysis. *Science* **343**, 1239176 (2014).
3 Romero, N. A. & Nicewicz, D. A. Organic photoredox catalysis. *Chem. Rev.* **116**, 10075–10166 (2016).
4 Meyer, F., Halasyamani, P. S. & Masson, G. Advances in organic and inorganic photoredox catalysis. *ACS Org. Inorg. Au* **3**, 1-3 (2023).
5 Staveness, D., Bosque, I. & Stephenson, C. R. J. Free radical chemistry enabled by visible light-induced electron transfer. *Acc. Chem. Res.* **49**, 2295–2306 (2016).
6 Kärkäs, M. D., Porco, J. A. & Stephenson, C. R. J. Photochemical approaches to complex chemotypes: applications in natural product synthesis. *Chem. Rev.* **116**, 9683–9747 (2016).
7 Lee, B. J., DeGlopper, K. S. & Yoon, T. P. Site-selective alkoxylation of benzylic C−H bonds by photoredox catalysis. *Angew. Chem., Int. Ed.* **59**, 197-202 (2020).
8 Xie, J. *et al.* Gold-catalyzed highly selective photoredox C(sp^2)−H difluoroalkylation and perfluoroalkylation of hydrazones. *Angew. Chem., Int. Ed.* **55**, 2934-2938 (2016).
9 Li, J. *et al.* Photoredox catalysis with aryl sulfonium salts enables site-selective late-stage fluorination. *Nat. Chem.* **12**, 56–62 (2020).
10 Wang, C. & Lu, Z. Catalytic enantioselective organic transformations via visible light photocatalysis. *Org. Chem. Front.* **2**, 179-190 (2015).
11 Huo, H. *et al.* Asymmetric photoredox transition-metal catalysis activated by visible light. *Nature* **515**, 100–103 (2014).
12 Tucker, J. W., Zhang, Y., Jamison, T. F. & Stephenson, C. R. J. Visible light photoredox catalysis in flow. *Angew. Chem., Int. Ed.* **51**, 4144-4147 (2012).
13 Su, Y., Straathof, N. J. W., Hessel, V. & Noël, T. Photochemical transformations accelerated in continuous-flow reactors: basic concepts and applications. *Chem. Eur. J.* **20**, 10562-10589 (2014).
14 Arias-Rotondo, D. M. & McCusker, J. K. The photophysics of photoredox catalysis: a roadmap for catalyst design. *Chem. Soc. Rev.* **45**, 5803-5820 (2016).
15 Speckmeier, E., Fischer, T. G. & Zeitler, K. A toolbox approach to construct broadly applicable metal-free catalysts for photoredox chemistry: deliberate tuning of redox potentials and importance of halogens in donor–acceptor cyanoarenes. *J. Am. Chem. Soc.* **140**, 15353–15365 (2018).
16 Bryden, M. A. & Zysman-Colman, E. Organic thermally activated delayed fluorescence (TADF) compounds used in photocatalysis. *Chem. Soc. Rev.* **50**, 7587-7680 (2021).
17 Glaser, F. & Wenger, O. S. Recent progress in the development of transition-metal based photoredox catalysts. *Coord. Chem. Rev.* **405**, 213129 (2020).
18 Yoon, T. P., Ischay, M. A. & Du, J. Visible light photocatalysis as a greener approach to photochemical synthesis. *Nat. Chem.* **2**, 527-532 (2010).
19 Marzo, L., Pagire, S. K., Reiser, O. & König, B. Visible-light photocatalysis: does it make a difference in organic synthesis? *Angew. Chem., Int. Ed.* **57**, 10034-10072 (2018).
20 Cocquet, G., Ferroud, C. & Guy, A. A mild and efficient procedure for ring-opening reactions of piperidine and pyrrolidine derivatives by single electron transfer photooxidation. *Tetrahedron* **56**, 2975-2984 (2000).
21 Lee, J., Papatzimas, J. W., Bromby, A. D., Gorobets, E. & Derksen, D. J. Thiaporphyrin-mediated photocatalysis using red light. *RSC Adv.* **6**, 59269-59272 (2016).
22 Yerien, D. E., Cooke, M. V., Vior, M. C. G., Barata-Vallejo, S. & Postigo, A. Radical fluoroalkylation reactions of (hetero)arenes and sulfides under red light photocatalysis. *Org. Biomol. Chem.* **17**, 3741-3746 (2019).
23 MeiJosé, L., Veleta, M. & Gianetti, T. L. Helical carbenium ion: a versatile organic photoredox catalyst for red-light-mediated reactions. *J. Am. Chem. Soc.* **142**, 12056–12061 (2020).

24 Ogura, A., Ichii, N., Shibata, K. & Takao, K.-i. Red-light-mediated Barton–McCombie reaction. *Bull. Chem. Soc. Jpn.* **93**, 936–941 (2020).
25 Watanabe, K. *et al.* Indolizines enabling rapid uncaging of alcohols and carboxylic acids by red light-induced photooxidation. *Org. Lett.* **22**, 5434–5438 (2020).
26 Whittemore, T. J., Xue, C., Huang, J., Gallucci, J. C. & Turro, C. Single-chromophore single-molecule photocatalyst for the production of dihydrogen using low-energy light. *Nat. Chem.* **12**, 180–185 (2020).
27 Ishikawa, Y. *et al.* Red-light-activatable ruthenium phthalocyanine catalysts. *Chem. Commun.* **57**, 13594-13597 (2021).
28 Buksh, B. F. *et al.* μMap-red: proximity labeling by red light photocatalysis. *J. Am. Chem. Soc.* **144**, 6154–6162 (2022).
29 Hu, X. *et al.* Red-light-driven atom transfer radical polymerization for high-throughput polymer synthesis in open air. *J. Am. Chem. Soc.* **145**, 24315–24327 (2023).
30 Chacktas, G. *et al.* Evidence of spin-forbidden excitation of $[Ru(bpy)_3]^{2+}$ and application in red-light-driven photocatalysis. *ACS Catal.* **15**, 13938–13947 (2025).
31 Kerzig, J. B. B. C., Larsen, C. B. & Wenger, O. S. A photorobust Mo(0) complex mimicking $[Os(2,2'\text{-bipyridine})_3]^{2+}$ and its application in red-to-blue upconversion. *J. Am. Chem. Soc.* **143**, 1651–1663 (2021).
32 Sinha, N., Wegeberg, C., Häussinger, D., Prescimone, A. & Wenger, O. S. Photoredox-active Cr(0) luminophores featuring photophysical properties competitive with Ru(II) and Os(II) complexes. *Nat. Chem.* **15**, 1730–1736 (2023).
33 Morselli, G., Eggenweiler, T. H., Villa, M., Prescimone, A. & Wenger, O. S. Pushing the thermodynamic and kinetic limits of near-infrared emissive Cr^{III} complexes in photocatalysis. *J. Am. Chem. Soc.* **147**, 28226–28240 (2025).
34 Wellauer, J. *et al.* Iron(III) complexes with luminescence lifetimes of up to 100 ns to enhance upconversion and photocatalysis. *J. Am. Chem. Soc.* **147**, 8760–8768 (2025).
35 Ravetz, B. D. *et al.* Development of a platform for near-infrared photoredox catalysis. *ACS Cent. Sci.* **6**, 2053–2059 (2020).
36 Ogbu, I. M., Bassani, D. M., Robert, F. & Landais, Y. Photocatalyzed decarboxylation of oxamic acids under near-infrared conditions. *Chem. Commun.* **58**, 8802-8805 (2022).
37 Goldschmid, S. L. *et al.* Overcoming photochemical limitations in metallaphotoredox catalysis: red-light-driven C–N cross-coupling. *J. Am. Chem. Soc.* **144**, 22409–22415 (2022).
38 Zhou, Z., Wang, Z., Blenko, A. L., Li, J. & Lin, W. Viologen covalent organic framework mediates near-infrared light-induced electron transfer for catalytic oxidative coupling reactions. *J. Am. Chem. Soc.* **147**, 10846–10852 (2025).
39 Katsurayama, Y. *et al.* Direct near infrared light–activatable phthalocyanine catalysts. *Chem. Eur. J.* **28**, e202103223 (2022).
40 Sellet, N., Sebbat, M., Elhabiri, M., Cormier, M. & Goddard, J.-P. Squaraines as near-infrared photocatalysts for organic reactions. *Chem. Commun.* **58**, 13759-13762 (2022).
41 Tanioka, M. *et al.* Bridged eosin Y: a visible and near-infrared photoredox catalyst. *Chem. Commun.* **58**, 7825-7828 (2022).
42 Sellet, N., Clement-Comoy, L., Elhabiri, M., Cormier, M. & Goddard, J.-P. Second generation of near-infrared cyanine-based photocatalysts for faster organic transformations. *Chem. Eur. J.* **29**, e202302353 (2023).
43 Glaser, F., Kerzig, C. & Wenger, O. S. Multi-photon excitation in photoredox catalysis: concepts, applications, methods. *Angew. Chem., Int. Ed.* **59**, 10266 –10284 (2020).
44 Ravetz, B. D. *et al.* Photoredox catalysis using infrared light via triplet fusion upconversion. *Nature* **565**, 343–346 (2019).
45 Lepori, M., Schmid, S. & Barham, J. P. Photoredox catalysis harvesting multiple photon or electrochemical energies. *Beilstein J. Org. Chem.* **19**, 1055-1145 (2023).
46 Wang, C., Wegeberg, C. & Wenger, O. S. First-row d^6 metal complex enables photon upconversion and initiates blue light-dependent polymerization with red light. *Angew. Chem., Int. Ed.* **62**, e202311470 (2023).
47 Kundu, B. K., Han, G. & Sun, Y. Derivatized benzothiazoles as two-photon-absorbing organic photosensitizers active under near infrared light irradiation. *J. Am. Chem. Soc.* **145**, 3535–3542

(2023).
48 Han, G. *et al.* Two-photon-absorbing ruthenium complexes enable near infrared light-driven photocatalysis. *Nat. Commun.* **13**, 2288 (2022).
49 Tay, N. E. S. *et al.* Targeted activation in localized protein environments via deep red photoredox catalysis. *Nat. Chem.* **15**, 101–109 (2023).
50 Tong, F., Zhou, W., Janiszewska, M. & Seath, C. P. Multiprobe photoproximity labeling of the EGFR interactome in glioblastoma using red-light. *J. Am. Chem. Soc.* **147**, 9316–9327 (2025).
51 Lou, Z. *et al.* Deep-red and ultrafast photocatalytic proximity labeling empowered in situ dissection of tumor-immune interactions in primary tissues. *J. Am. Chem. Soc.* **147**, 9716–9726 (2025).
52 Yang, W. *et al.* Manganese low-energy photocatalysis for remodeling nitrogenation of alkenes. *Chem Catal.* **12**, 102702 (2026).
53 Chen, X., Liu, L., Yu, P. Y. & Mao, S. S. Increasing solar absorption for photocatalysis with black hydrogenated titanium dioxide nanocrystals. *Science* **331**, 746-750 (2011).
54 Zhu, M. *et al.* Metal-free photocatalyst for H_2 evolution in visible to near-infrared region: black phosphorus/graphitic carbon nitride. *J. Am. Chem. Soc.* **139**, 13234–13242 (2017).
55 Atta, S., Pennington, A. M., Celik, F. E. & Fabris, L. TiO_2 on gold nanostars enhances photocatalytic water reduction in the near-infrared regime. *Chem* **4**, 2140-2153 (2018).
56 Pak, K., Cheung, S., Sarkar, S. & Gevorgyan, V. Visible light-induced transition metal catalysis. *Chem. Rev.* **122**, 1543–1625 (2021).
57 Sinha, N. & Wenger, O. S. Photoactive metal-to-ligand charge transfer excited states in $3d^6$ complexes with Cr^0, Mn^I, Fe^{II}, and Co^{III}. *J. Am. Chem. Soc.* **145**, 4903–4920 (2023).
58 Büldt, L. A. & Wenger, O. S. Chromium(0), molybdenum(0), and tungsten(0) isocyanide complexes as luminophores and photosensitizers with long-lived excited states. *Angew. Chem., Int. Ed.* **56**, 5676-5682 (2017).
59 Ashford, D. L. *et al.* Controlling ground and excited state properties through ligand changes in ruthenium polypyridyl complexes. *Inorg. Chem.* **53**, 5637–5646 (2014).
60 You, Y. & Park, S. Y. Inter-ligand energy transfer and related emission change in the cyclometalated heteroleptic iridium complex: facile and efficient color tuning over the whole visible range by the ancillary ligand structure. *J. Am. Chem. Soc.* **127**, 12438–12439 (2005).
61 Chábera, P. *et al.* A low-spin Fe(III) complex with 100-ps ligand-to-metal charge transfer photoluminescence. *Nature* **543**, 695–699 (2017).
62 Yaltseva, P., Maisuradze, T., Prescimone, A., Kupfer, S. & Wenger, O. S. Structural control of metal-centered excited states in cobalt(III) complexes via bite angle and π–π interactions. *J. Am. Chem. Soc.* **147**, 29444–29456 (2025).
63 Cuttell, D. G., Kuang, S.-M., Fanwick, P. E., McMillin, D. R. & Walton, R. A. Simple Cu(I) complexes with unprecedented excited-state lifetimes. *J. Am. Chem. Soc.* **124**, 6–7 (2002).
64 Morselli, G., Reber, C. & Wenger, O. S. Molecular design principles for photoactive transition metal complexes: a guide for "photo-motivated" chemists. *J. Am. Chem. Soc.* **147**, 11608–11624 (2025).
65 Sinha, N., Yaltseva, P. & Wenger, O. S. The nephelauxetic effect becomes an important design factor for photoactive first-row transition metal complexes. *Angew. Chem., Int. Ed.* **62**, e202303864 (2023).
66 Larsen, C. B. *et al.* Metal–ligand covalency in the valence excited states of metal dithiolenes revealed by S 1s3p resonant inelastic X-ray scattering. *J. Am. Chem. Soc.* **146**, 28561–28571 (2024).
67 Bürgin, T. H., Glaser, F. & Wenger, O. S. Shedding light on the oxidizing properties of spin-flip excited states in a Cr^{III} polypyridine complex and their use in photoredox catalysis. *J. Am. Chem. Soc.* **144**, 14181–14194 (2022).
68 Juban, E. A., Smeigh, A. L., Monat, J. E. & McCusker, J. K. Ultrafast dynamics of ligand-field excited states. *Coord. Chem. Rev.* **250**, 1783-1791 (2006).
69 Zhang, Y., He, G., Hou, S., Huang, Q. & Xia, C. Visible-light-driven Fischer-type indole synthesis: direct synthesis of 2-phosphinoylindoles from anilines. *Org. Lett.* **27**, 6676–6681 (2025).
70 Leitch, J. A., Rossolini, T., Rogova, T., Maitland, J. A. P. & Dixon, D. J. α-Amino radicals via photocatalytic single-electron reduction of imine derivatives. *ACS Catal.* **10**, 2009–2025 (2020).
71 Choi, W. J. *et al.* Mechanisms and applications of cyclometalated Pt(II) complexes in photoredox catalytic trifluoromethylation. *Chem. Sci.* **6**, 1454-1464 (2015).
72 Xiong, L. & Tang, J. Strategies and challenges on selectivity of photocatalytic oxidation of organic substances. *Adv. Energy Mater.* **11**, 2003216 (2021).

73 Bhandari, A. *et al.* A stable radical within a N–Co–N core. *Chem. Commun.* **60**, 9970-9973 (2024).
74 Lu, T. & Chen, F. Multiwfn: A multifunctional wavefunction analyzer. *Comput. Chem.* **33**, 580 (2012).
75 Liu, Z. & Lu, T. An sp-hybridized all-carboatomic ring, cyclo[18]carbon: Electronic structure, electronic spectrum, and optical nonlinearity. *Carbon* **165**, 461-467 (2020).
76 Neugebauer, H., Bohle, F., Bursch, M., Hansen, A. & Grimme, S. Benchmark study of electrochemical redox potentials calculated with semiempirical and DFT methods. *J. Phys. Chem. A* **124**, 7166–7176 (2020).
77 Marenich, A. V., Ho, J., Coote, M. L., Cramer, C. J. & Truhlar, D. G. Computational electrochemistry: prediction of liquid-phase reduction potentials. *Phys. Chem. Chem. Phys.* **16**, 15068-15106 (2014).
78 Truhlar, D. G., Cramer, C. J., Lewis, A. & Bumpus, J. A. Molecular modeling of environmentally important processes: reduction potentials. *J. Chem. Educ.* **81**, 596-604 (2004).

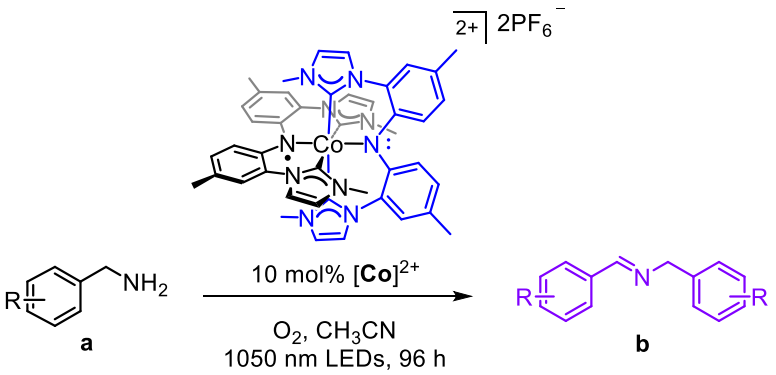
Table 1. NIR-activatable Photocatalysis. Oxidative coupling reactions of benzylamine under various conditions[a]



Entry	Photoirradiation wavelength (nm) / Power (mW)	Conversion (%)[b]	Yield (%)[c]	ε (10^4 M^{-1} cm^{-1})[d]	Φ_r (%)[e]
1	1050 (340)	75[f]	70[f]	0.02	0.4
2	405 (1400)	99[g]	96[g]	0.38	0.001
3	650 (700)	99[g]	95[g]	0.18	0.1
4	850 (104)	99[f]	92[f]	0.08	0.9
5	2800 (50)	N.D.[f,h]	N.D.[f,h]	0.39	N.D.[f,h]
Variations on entry 1					
6	Ar instead of O_2	trace[f]	trace[f]		
7	No photon source	N.D.[f,h]	N.D.[f,h]		
8	No $[\mathbf{Co}]^{2+}$ catalyst	N.D.[f,h]	N.D.[f,h]		

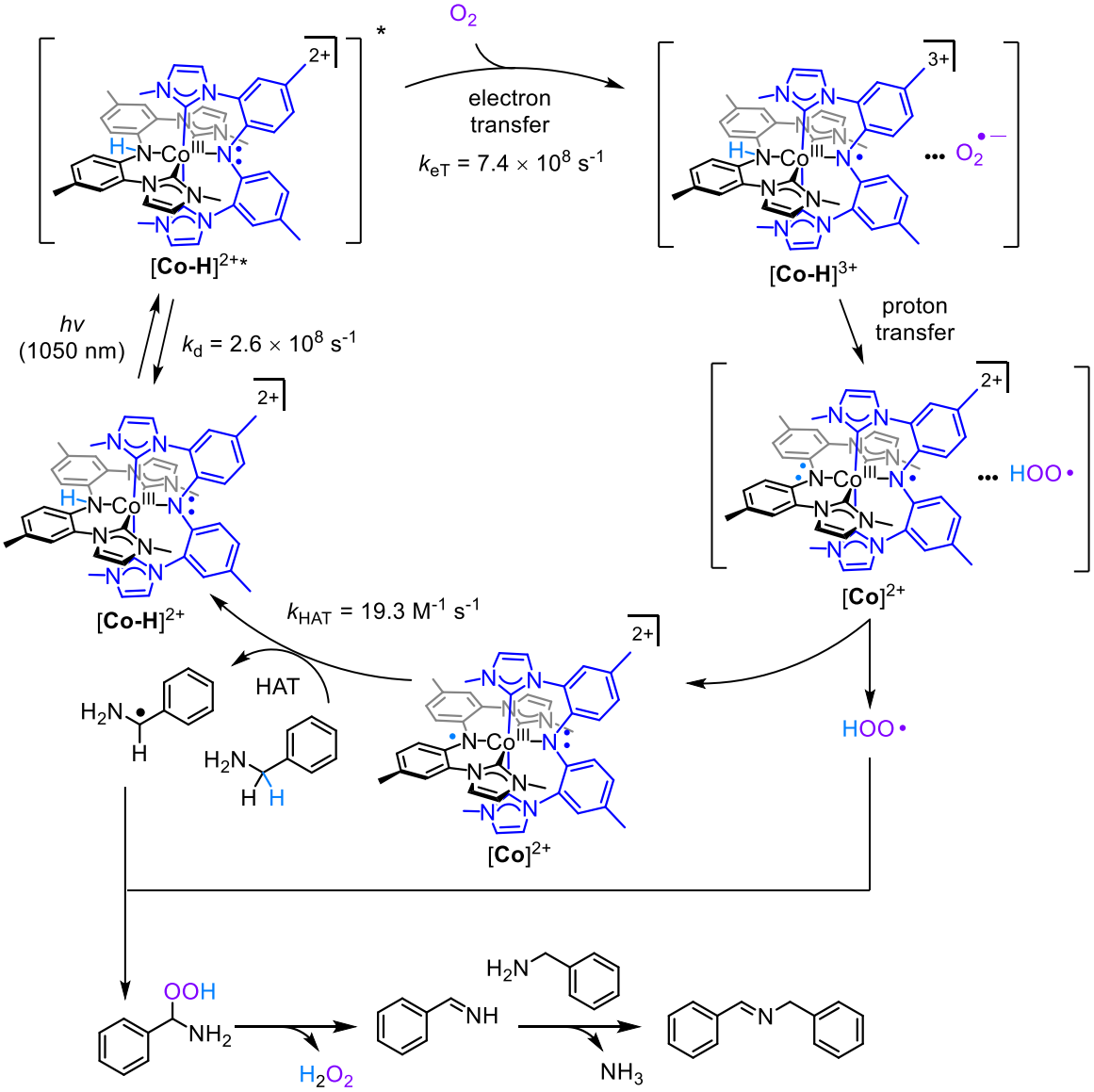
[a]Reaction scale: **1a** (0.1 mmol), CH_3CN (0.1 M, 1.0 mL). [b]Conversion was determined by gas chromatography using *n*-dodecane as an internal standard. [c]Isolated yields. [d]Molar absorbance at the photoexcitation wavelength of $[\mathbf{Co}]^{2+}$. [e]Quantum yields for the reaction. [f]14 day-reaction time. [g]24 h-reaction time. [h]Not determined.

Table 2. Reaction scope. Scope of the NIR light-driven photocatalytic oxidative coupling reactions of benzylamines[a]



a	b (conversion / yield)	a	b (conversion / yield)
1a	**1b** (81% / 75%)	**8a**	**8b** (75% / 52%)
2a	**2b** (60% / 54%)	**9a**	**9b** (83% / 80%)
3a	**3b** (63% / 57%)	**10a**	**10b** (78% / 70%)
4a	**4b** (76% / 63%)	**11a**	**11b** (67% / 61%)
5a	**5b** (51% / 40%)	**12a**	**12b** (63% / 58%)
6a	**6b** (88% / 83%)	**13a**	**13b** (69% / 60%)
7a	**7b** (81% / 70%)	**14a**	**14b** (36% / 21%)

[a]Reaction conditions: **a** (0.05 mmol), $[\mathbf{Co}]^{2+}$ (10 mol %), CH_3CN (0.1 M, 0.5 mL), an O_2 atmosphere, and 1050-nm LEDs (340 mW). Yields were determined by ^1H NMR spectroscopy using bromoform as an internal standard.



Scheme 1. Plausible photocatalysis mechanism.

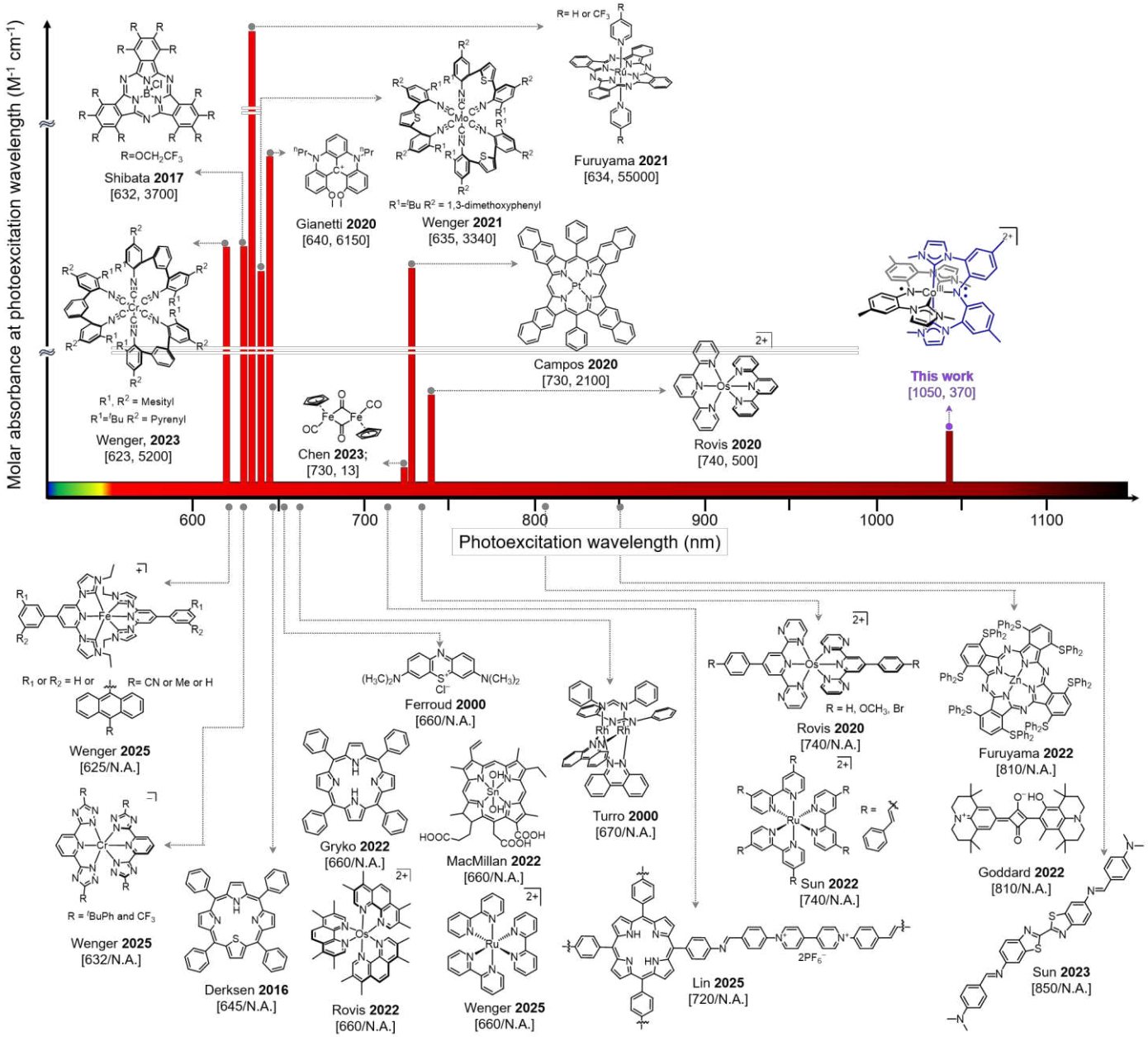


Figure 1. Long-wavelength-activatable photocatalysts. The chemical structures, photoactivation wavelengths, and molar absorbance at the photoactivation wavelength of previously reported long-wavelength-activatable molecular photocatalysts. The two values in parentheses correspond to the photoactivation wavelength and the molar absorbance at the photoactivation wavelength. No molar absorbance at the photoexcitation wavelength was reported for the catalysts shown at the bottom of the figure.

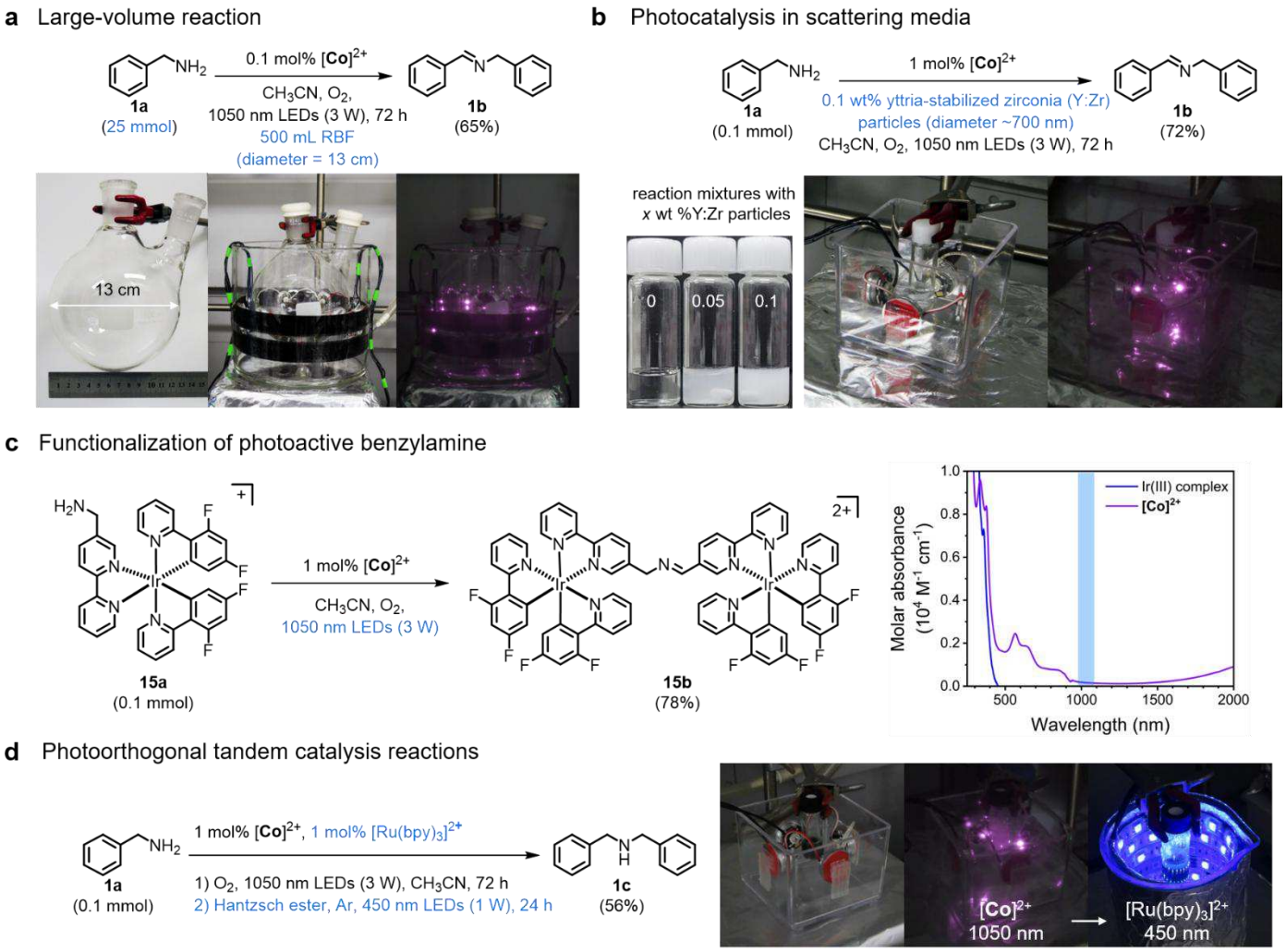


Figure 2. NIR photocatalysis. a, Large-volume photocatalytic oxidative coupling reaction of **1a** performed in a 500-mL round-bottom flask under illumination at 1050 nm. The photos show the reaction flask and the reaction set-up under ambient light and 1050-nm LEDs photoirradiation. **b**, Photocatalytic oxidative coupling reaction of **1a** in the presence of light-scattering yttria-stabilized zirconia particles (size ~ 700 nm). The photos show the reaction media at three concentrations of yttria-stabilized zirconia particles (0, 0.05, and 0.1 wt%) and the reaction set-up under ambient light and 1050-nm LEDs photoirradiation. **c**, NIR-photocatalytic oxidative coupling reaction of a Vis-active Ir(III) complex tethering an aminomethylene substituent (**15a**). The right graph compares the UV–Vis–NIR absorption spectra of $[\mathbf{Co}]^{2+}$ and **15a**. The blue-shaded region indicates the photoirradiation region. **d**, Photoorthogonal tandem catalysis reaction of **1a**. The reaction mixture contained dual $[\mathbf{Co}]^{2+}$ (1 mol%) and $[Ru(bpy)_3]^{2+}$ (1 mol%) photocatalysts, and was illuminated at 1050 nm, followed by 450 nm in the presence of a Hantzsch ester. The photos show the reactor under ambient light (left) and 1050-nm (middle) and 450-nm (right) photoirradiation.

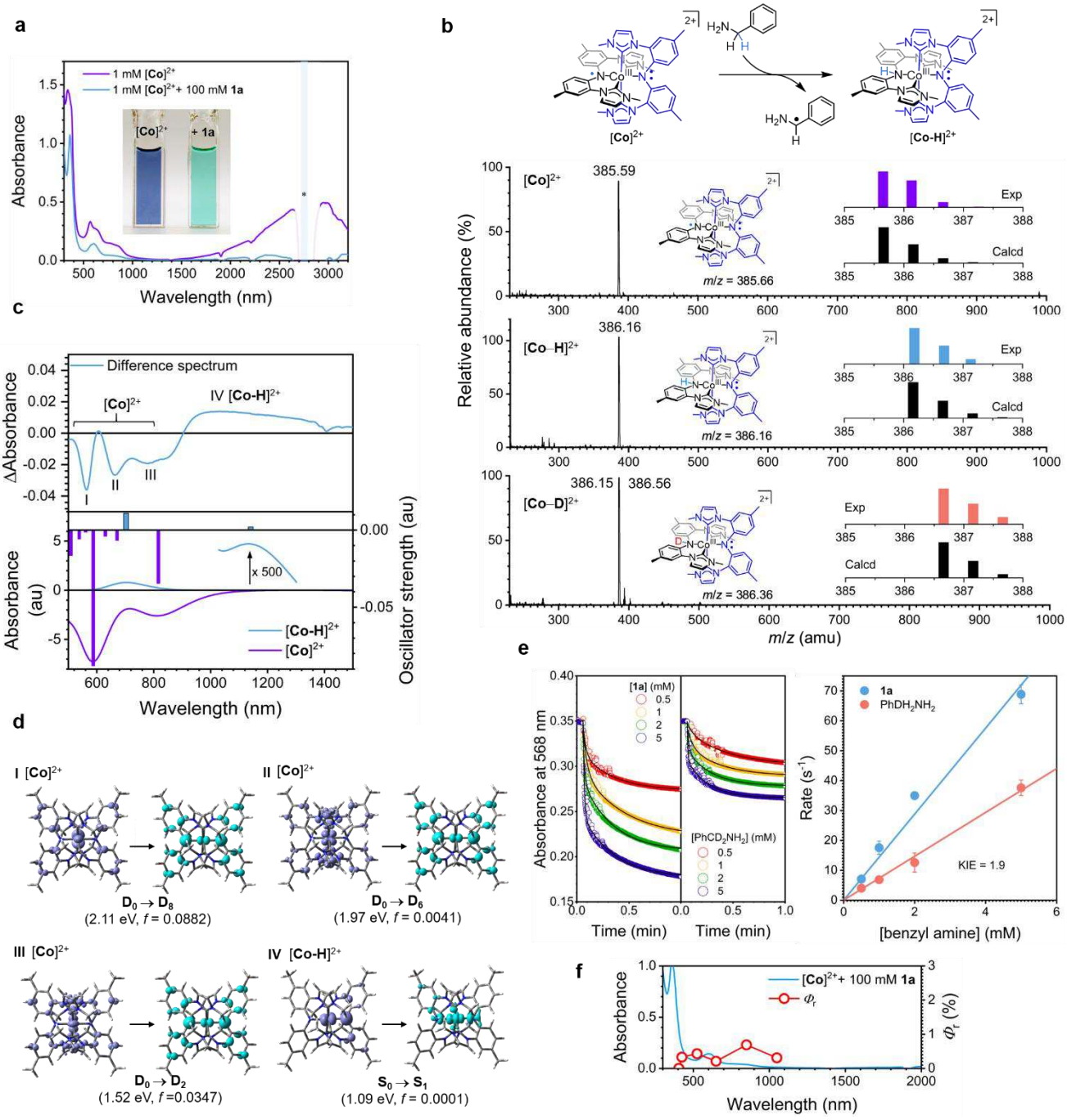


Figure 3. Photocatalytic species. a, Vis–NIR absorption spectra of 1.0 mM [**Co**]$^{2+}$ in aerated CD_3CN before and after the addition of 100 mM **1a**. The cyan region marked with an asterisk is due to the vibrational overtone and combination band absorption of the solvent. **b,** Mass spectra (electrospray ionization, positive mode) of [**Co**]$^{2+}$ in the absence (top) and presence of **1a** (middle) and $PhCD_2NH_2$ (bottom). **c**, Top, difference spectrum of Vis–NIR absorption spectra of 1.0 mM [**Co**]$^{2+}$ before and after the addition of 100 mM **1a**; bottom, quantum chemically simulated electronic transition spectra for [**Co–H**]$^{2+}$ and [**Co**]$^{2+}$. The vertical bars are oscillator strengths. **d**, Isosurface plots (isovalue = 0.01) of natural transition orbitals for the electronic transitions marked with I–IV in **c**. **e,** Left, primary kinetic isotope effects of [**Co**]$^{2+}$ with **1a** and $PhCD_2NH_2$; right, corresponding pseudo-first order plots. **f**, An overlay of the Vis–NIR absorption spectrum of 1.0 mM [**Co**]$^{2+}$ in the presence of 100 mM **1a** and the quantum yield for the reaction (Φ_r).

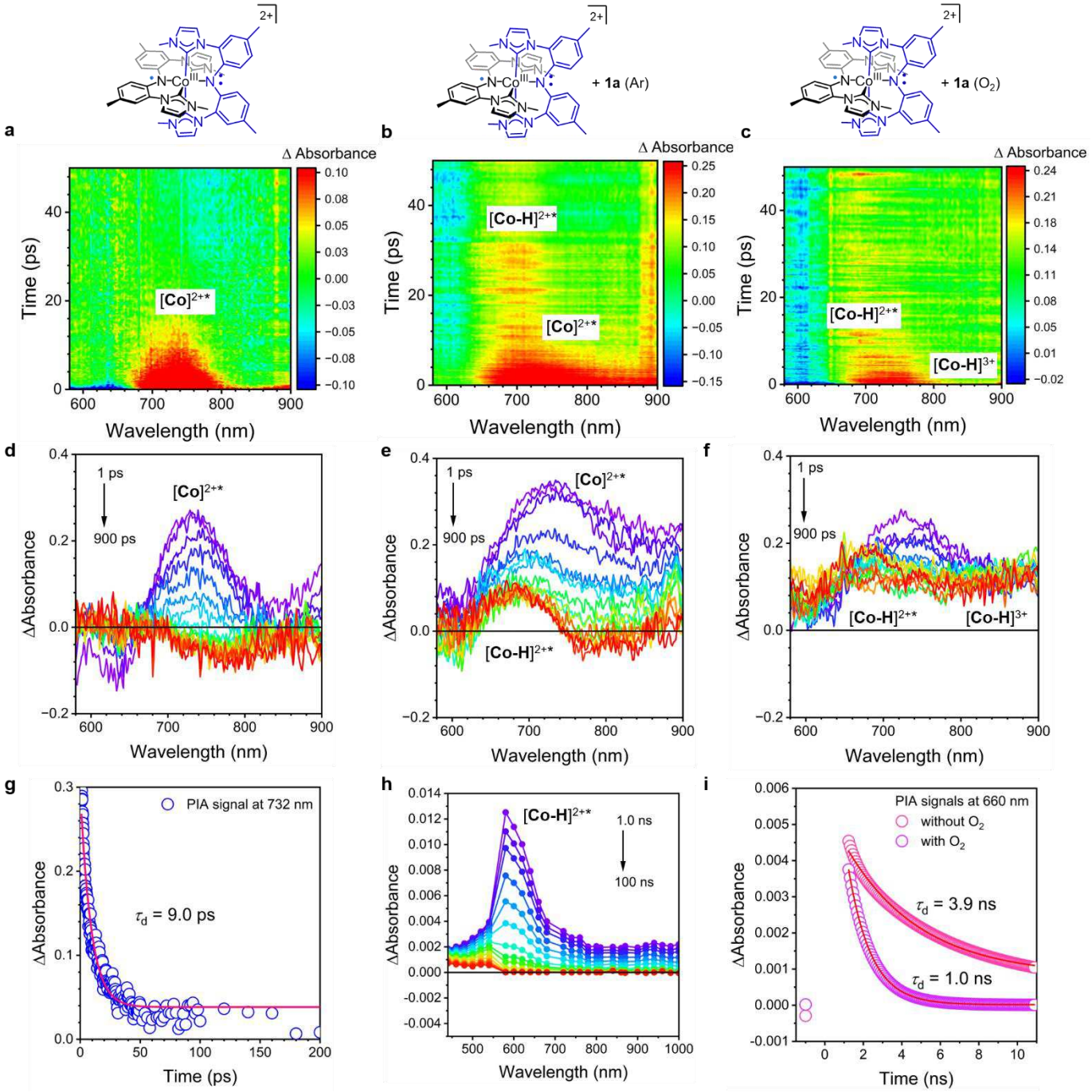


Figure 4. Photocatalysis processes. a–c, Heatmaps of transient absorption signals of (**a**) 2.0 mM [**Co**]$^{2+}$ and mixtures of 2.0 mM [**Co**]$^{2+}$ and 200 mM **1a** in the absence (**b**) and presence (**c**) of O_2 recorded after femtosecond pulsed laser photoexcitation at 550 nm (CH_3CN). **d–f,** Selected transient absorption spectra of (**d**) 2.0 mM [**Co**]$^{2+}$ and mixtures of 2.0 mM [**Co**]$^{2+}$ and 200 mM **1a** in the absence (**e**) and presence (**f**) of O_2 recorded after femtosecond pulsed laser photoexcitation at 550 nm (CH_3CN). **g,** The decay profile of the PIA signals for 2.0 mM [**Co**]$^{2+}$ (λ_{obs} = 732 nm). The red curve is a nonlinear least-squares fit to a monoexponential decay model (R^2 = 0.95). **h,** Selected transient absorption spectra of a mixture of 2.0 mM [**Co**]$^{2+}$ and 200 mM **1a** in the absence of O_2 recorded after nanosecond pulsed laser photoexcitation at 532 nm (CH_3CN). **i,** Decay traces of PIA signals of mixtures of 2.0 mM [**Co**]$^{2+}$ and 200 mM **1a** in the absence and presence of O_2, recorded after nanosecond pulsed laser photoexcitation. Red curves are nonlinear least-squares fits to a monoexponential decay model ($R^2 > 0.99$).

Supplementary Files

This is a list of supplementary files associated with this preprint. Click to download.

- Supplementaryinformation.pdf